CHEMISTRY OF MATERIALS
Cite This: Chem. Mater. 2019, 31, 3756–3765
Article
pubs.acs.org/cm

Understanding the Low-Voltage Hysteresis of Anionic Redox in $Na_2Mn_3O_7$

Bohang Song,[†,▲] Mingxue Tang,[‡,§,∥,▲] Enyuan Hu,[⊥] Olaf J. Borkiewicz,[#] Kamila M. Wiaderek,[#] Yiman Zhang,[¶] Nathan D. Phillip,[¶,▽] Xiaoming Liu,[○] Zulipiya Shadike,[⊥] Cheng Li,[♦] Likai Song,[‡,§] Yan-Yan Hu,[‡,§] Miaofang Chi,[○] Gabriel M. Veith,[¶] Xiao-Qing Yang,[⊥] Jue Liu,[*,†] Jagjit Nanda,[*,¶,▽] Katharine Page,[*,†] and Ashfia Huq[*,†]

[†]Neutron Scattering Division, [¶]Chemical Sciences Division, [○]Center for Nanophase Materials Sciences Division, and [♦]Juelich Center for Neutron Science, Outstation at the Spallation Neutron Source, Oak Ridge National Laboratory, Oak Ridge, Tennessee 37831, United States

[‡]Florida State University, Tallahassee 32306, United States

[§]National High Magnetic Field Laboratory, Tallahassee 32310, United States

[∥]Center for High Pressure Science and Technology Advanced Research, Beijing 100094, China

[⊥]Chemistry Division, Brookhaven National Laboratory, Upton, New York 11973, United States

[#]X-ray Science Division, Advanced Photon Source, Argonne National Laboratory, Argonne 60439, Illinois, United States

[▽]Bredesen Center for Interdisciplinary Research and Graduate Education, University of Tennessee, Knoxville, Tennessee 37996, United States

Supporting Information

ABSTRACT: The large-voltage hysteresis remains one of the biggest barriers to optimizing Li/Na-ion cathodes using lattice anionic redox reaction, despite their very high energy density and relative low cost. Very recently, a layered sodium cathode $Na_2Mn_3O_7$ (or $Na_{4/7}Mn_{6/7}\square_{1/7}O_2$, $\square$ is vacancy) was reported to have reversible lattice oxygen redox with much suppressed voltage hysteresis. However, the structural and electronic structural origin of this small-voltage hysteresis has not been well understood. In this article, through systematic studies using ex situ/in situ electron paramagnetic resonance and X-ray diffraction, we demonstrate that the exceptional small-voltage hysteresis (<50 mV) between charge and discharge curves is rooted in the well-maintained oxygen stacking sequence in the absence of irreversible gliding of oxygen layers and cation migration from the transition-metal layers. In addition, we further identify that the 4.2 V charge/discharge plateau is associated with a zero-strain (de)intercalation process of Na^+ ions from distorted octahedral sites, while the 4.5 V plateau is linked to a reversible shrink/expansion process of the manganese-site vacancy during (de)intercalation of Na^+ ions at distorted prismatic sites. It is expected that these findings will inspire further exploration of new cathode materials that can achieve both high energy density and efficiency by using lattice anionic redox.

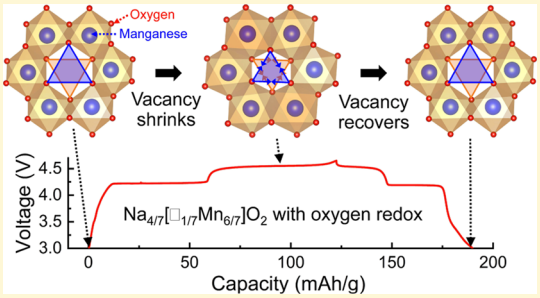

INTRODUCTION

The charge storage of conventional intercalation-based cathodes is achieved by the extraction/intercalation of Li^+/Na^+ ions in concomitance with the oxidation/reduction of transition metal (TM) cations. Therefore, the capacities of these cathodes are often limited by the amount of TM redox couples. Recently, a class of lithium-excess materials (with lithium partially replacing TM cations on the TM layers) have attracted broad interest because of their high specific capacity enabled by both cation and lattice oxygen redox couples.[1−8] However, the large voltage hysteresis (>500 mV) between charge and discharge curves leads to relatively low energy efficiency, together with a large content of irreversible oxygen redox, hindering the optimization of this type of cathode material. In the last decade, there have been extensive efforts to reduce the voltage hysteresis and minimize the subsequent voltage decay of Li-excess material via cation doping or surface modification.[9,10] However, progress remains relatively limited and the basic requirements for commercial grade technologies remain unfulfilled. Therefore, much effort has been devoted to exploring novel cathode systems where intrinsic reversible oxygen redox chemistry can be realized with minimized voltage hysteresis. In order to stabilize the cathode structure upon electrochemical cycling including lattice oxygen redox, 4d and

Received: February 22, 2019
Revised: April 25, 2019
Published: May 1, 2019

DOI: 10.1021/acs.chemmater.9b00772
Chem. Mater. 2019, 31, 3756–3765

5d TMs (such as Ir and Ru) have been introduced to both lithium ion batteries and sodium ion batteries (SIBs).[11,12] It is thus important and timely to extend these concepts to the low-cost 3d TM-based cathodes. More recently, reversible lattice oxygen redox with very small voltage hysteresis (~200 mV) has been observed in the P3-type $Na_{0.6}Li_{0.2}Mn_{0.8}O_2$.[13,14] Real reversible oxygen redox in this system can be ascribed to two aspects: first, the large interlayer spacing occupied by Na^+ is very unfavorable for Mn^{4+} due to its small ionic radii (0.53 Å, eight-coordinated),[15] effectively preventing TM cation migration and irreversible gliding of oxygen layers at deep charge states and, second, the presence of relatively narrow oxygen 2p bands corresponding to the nearly unhybridized oxygen 2p orbitals of the Na−O−Li or □−O−Li configuration, leading to very flat charge/discharge plateaus.[16] This inspires us to search for other sodium-ion cathodes that may possess similar reversible oxygen redox capability.

It is generally believed that one (of three) oxygen 2p orbitals is nearly unhybridized in the Li−O−Li (or Na) configuration in the layered (or rock-salt) Li(Na)TMO_2 due to the large energy difference between the Li 1s and O 2p orbitals, or the very strong ionic nature of the Na−O bonds. Thus, if Li^+ ions on the TM layer are replaced by vacancies, the degree of orbital overlapping is expected to be further decreased, especially in the fully charged state (when large amounts of interlayer Na^+ are removed). Thus, narrower nonbonding oxygen 2p states can be created in the vacancy-rich layered sodium oxides in both charged and discharged states. Although creating large amounts of vacancies on the TM layers is generally believed to be a thermodynamically unfavorable process, a few natural phyllomanganite minerals have been reported to possess appreciable amounts of Mn vacancies, such as chalcophanite ($ZnMn_3O_7{\cdot}H_2O$ or $Zn_{2/7}Mn_{6/7}\square_{1/7}O_2{\cdot}H_2O$, Figure S1).[17] More recently, we and others also demonstrated that vacancy-rich sodium or copper analogues of the mineral chalcophanite can be synthesized via soft methods at relatively low temperatures.[18] These discoveries encourage us to explore the plausibility to achieve TM vacancy induced lattice oxygen redox activity in this family of compounds. Moreover, very recently, several groups reported that nonbonding 2p orbitals of oxygens neighbored by the Mn vacancies within $Na_{4/7-x}[Mn_{6/7}\square_{1/7}]O_2$ contribute to the oxygen-redox capacity without making the Mn−O bond labile.[19−21] Surprisingly, the voltage hysteresis is relatively small compared to most of other electrode materials harvesting oxygen-redox capacity. Nonetheless, it is still unclear why the oxygen redox is highly reversible in this system with exceptionally small voltage hysteresis in the view of the evolutional changes in the crystal structure and the electronic structure upon (de)sodiation. In this report, we will show detailed experimental evidence on the reversible oxygen redox activity induced by TM vacancy, with specific attention paid to the structural evolution upon (de)sodiation of $Na_{4/7-x}[Mn_{6/7}\square_{1/7}]O_2$ and its impact on the lattice oxygen redox reaction.

EXPERIMENTAL SECTION

Preparation of $Na_2Mn_3O_7$. Phase pure $Na_2Mn_3O_7$ was synthesized using a conventional solid-state reaction.[22] $NaNO_3$ (J. T. Baker, A.C.S. Reagent) and $MnCO_3$ (Aldrich, ≥99.9%) were first mixed in stoichiometric amounts and the precursor was thoroughly ball-milled for 1 h, followed by heating at 600 °C for 12 h under an oxygen flow. Dark brown powders were obtained as a final product after naturally cooling down to room temperature (RT).

Electrochemical Testing. The as-prepared $Na_2Mn_3O_7$ powder was mixed with carbon black (Super P) and polyvinylidene fluoride in a weight ratio of 8:1:1 using *N*-methyl-2-pyrrolidone as solvent. The slurry was then cast onto an aluminum foil before drying overnight at 120 °C in a vacuum oven. The loading density of working electrode (diameter ≈ 1.1 cm) is typically ~2−3 mg cm^{-2}. The electrochemical performance was tested using coin cells (size CR2032, Hohsen Corp. Japan) by assembling the working electrode, Na disk, and separator (Celgard 2325) soaked in Na electrolyte in an argon-filled glovebox. The electrolyte contains 1 M $NaClO_4$ dissolved in propylene carbonate (PC) and fluoroethylene carbonate (FEC) in a volume ratio of 98:2. The theoretical capacity was set to 150 mA h g^{-1} and electrochemical window to 3.0−4.65 V (vs Na^+/Na) unless otherwise specified. For all ex situ electrodes, the cells were charged to 4.2, 4.4, and 4.65 V, respectively, or first charged to 4.65 V and then discharged to 4.4, 4.2, and 3.0 V, respectively. All cells were held for at least 6 h when reaching the setup voltage before disassembly in the argon-filled glovebox. Note that all as-collected electrodes were not washed to avoid unexpected reactions.

Structure Characterizations. High-resolution synchrotron X-ray diffraction (XRD) data were collected at beamline 11-BM at Argonne National Laboratory with a wavelength of 0.412748 Å. Rietveld refinement was carried out using the fundamental parameters approach in TOPAS software (version 6).[23,24] High-resolution transmission electron microscopy (HRTEM) was performed using an aberration-corrected FEI Titan S 80-300 scanning TEM/TEM microscope equipped with a Gatan OneView camera at an accelerating voltage of 300 kV. RT neutron total scattering data were collected at the NOMAD beamline at the Spallation Neutron Source (SNS) at ORNL.[25] About 0.4 g powder sample was loaded into a 3 mm quartz capillary. Four ~30 min scans were collected and then summed together to improve the statistics. The detectors were calibrated using scattering from a diamond powder standard prior to the measurements. Neutron powder data were normalized against a V rod and the background was subtracted. The total scattering structure factor $S(Q)$ data were then transformed to PDF data $G(r)$ using the specific IDL codes developed for the NOMAD instrument with a Q range of 0.5−25.0 $Å^{-1}$. For small-box least square refinement, the instrument parameters dQ and Q_{broad} were determined to be 0.046 Å and 0.030 $Å^{-2}$ from the refinement of the PDF pattern of standard NIST Si-640e. The empirical PDFgui-type $\delta 1$ ($\delta 1/r$) term was used to model correlated motion effects with the refined $\delta 1$ being 1.30(9) Å.[26−28]

X-ray Absorption Spectroscopy and X-ray Photoelectron Spectroscopy. X-ray absorption spectroscopy (XAS) measurements were performed at the 8-ID beamline of the National Synchrotron Light Source II (NSLS II) at Brookhaven National Laboratory (BNL) in transmission mode. The X-ray absorption near edge structure (XANES) and extended X-ray absorption fine structure (EXAFS) spectra were processed using the Athena software package.[29] The AUTOBK code was used to normalize the absorption coefficient and separate the EXAFS signal, $\chi(k)$, from the isolated atom-absorption background. The extracted EXAFS signal, $\chi(k)$, was weighted by k^2 to emphasize the high-energy oscillations and then Fourier-transformed in a k range from 3.0 to 13.6 $Å^{-1}$ to analyze the data in R-space.

X-ray photoelectron spectroscopy (XPS) measurements were collected on a PHI 3056 XPS spectrometer with a Mg Kα (1253.6 eV) X-ray source operated at 15 kV and 350 W. Samples were transferred under vacuum from an argon-filled glovebox to a cryo-pumped vacuum chamber for measurements at 10^{-9} Torr or less (10^{-11} Torr base pressure). Survey scans were collected at 93.9 eV pass energy with 0.5 eV energy steps while high resolution scans were acquired at 23.5 eV pass energy and 0.05 eV energy steps. All spectra were collected for 20−60 repeats to improve the signal to noise ratio. Spectra were calibrated relative to the adventitious carbon peak (284.8 eV) to correct for minor charging.

Electron Paramagnetic Resonance. The cycled electrodes were dried under vacuum at RT for an extra 6 h before sealing in air-tight plastic bags under an argon atmosphere and then transferred for electron paramagnetic resonance (EPR) measurements. To check

DOI: 10.1021/acs.chemmater.9b00772
Chem. Mater. 2019, 31, 3756−3765

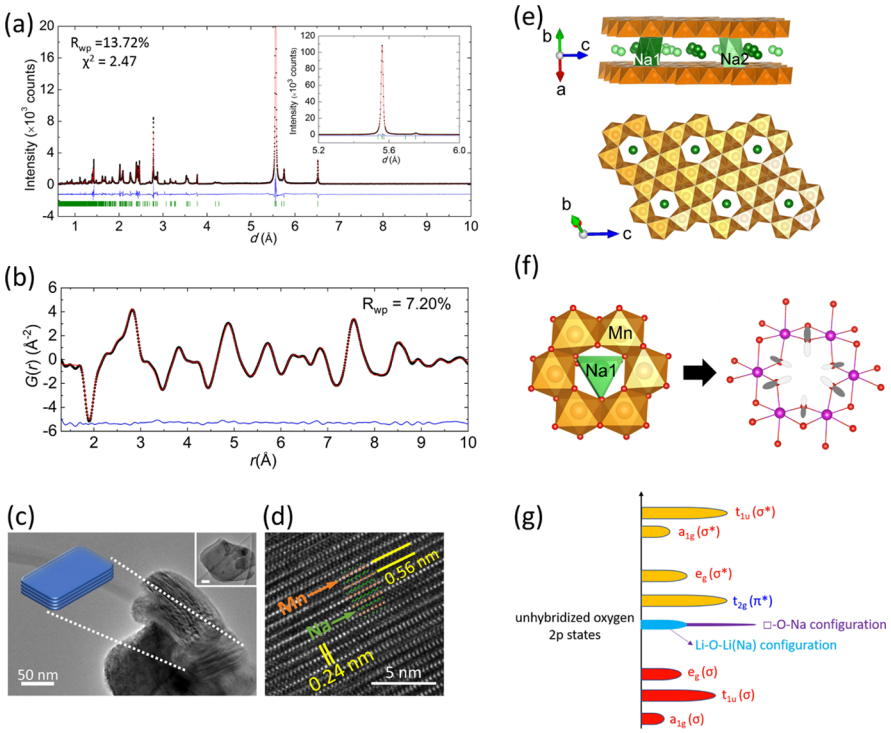

Figure 1. (a) Rietveld refinement of the structure of $Na_2Mn_3O_7$ using high-resolution synchrotron XRD (λ = 0.412748 Å), the experimental data are shown in black dots, calculated curve in red, and difference curve in blue. The Bragg reflection positions are marked with olive markers. (b) Least square refinement of the local structure $Na_2Mn_3O_7$ using short-range neutron pair distribution function data (1−10 Å). The experiment data are shown in black dots, calculated curve in red, and difference curve in blue. (c) TEM and (d) HRTEM images of the as-synthesized $Na_2Mn_3O_7$. The stacking plates in (c) highlights the 2D-like morphology of $Na_2Mn_3O_7$ due to the large *d*-spacing of the layered structure. (e) Refined structure of $Na_2Mn_3O_7$ with Mn shown in orange, Na in green and O in red. Na1 ions occupy the distorted prismatic sites above vacancies and Na2 ions occupy the distorted octahedral sites. (f) Local coordination environment for Na1 ion and the vacancy presented above on the TM layer. The right side shows the orphaned oxygen 2p orbitals point toward the vacancy site. The other two mutual oxygen 2p orbitals (which shall point toward the two neighboring TM) are omitted for clarity. (g) Band structure of layered sodium TM oxides with honeycomb-type vacancy. The unhybridized oxygen 2p bands (purple-colored) are expected to be much narrower in the present □−O−Na or □−O−□ configuration relative to the Li−O−Li (or Na) configuration in the conventional layered lithium-excess or sodium-excess TM oxides.

Table 1. Refined Structure of $Na_2Mn_3O_7$ Using Synchrotron XRD (λ = 0.412748 Å)

S.G. $P\bar{1}$	a = 6.6041(1) Å, b = 6.8506 (1) Å, c = 7.5266(1) Å, α = 106.188(3)°, β = 106.632(3)°, γ = 111.646(1)°					
site	Wyck.	x	y	z	occ.	B_{iso} (Å^2)
Mn1	2i	0.0730(5)	0.0737(4)	0.2236(4)	1	0.20(1)
Mn2	2i	0.3632(5)	0.3657(4)	0.0860(4)	1	0.20(1)
Mn3	2i	0.2238(4)	0.2250(4)	0.6455(4)	1	0.20(1)
Na1	2i	0.2440(8)	0.6985(8)	0.5059(8)	1	1.50(10)
Na2	2i	0.3264(10)	0.8216(9)	0.0803(9)	1	1.50(10)
O1	2i	0.3883(17)	0.2072(15)	0.2380(15)	1	0.50(6)
O2	2i	0.2678(17)	0.0873(14)	0.8341(18)	1	0.50(6)
O3	2i	0.0284(16)	0.2123(16)	0.0306(16)	1	0.50(6)
O4	2i	0.1251(15)	0.3235(14)	0.4401(15)	1	0.50(6)
O5	2i	0.6912(17)	0.5071(17)	0.1136(16)	1	0.50(6)
O6	2i	0.1167(14)	0.9384(16)	0.4111(14)	1	0.50(6)
O7	2i	0.4531(15)	0.6368(13)	0.2944(13)	1	0.50(6)

their structural stability, EPR measurements were performed for the same sealed samples after being stored in the argon-filled glovebox for an additional 7 days. Continuous-wave EPR (CW-EPR) spectra were acquired on a Bruker Elexsys E680 spectrometer in X-band (9.4 GHz) (Bruker BioSpin, Billerica, MA), using a high sensitivity cavity (ER 4119HS). The recording window was set to 500 mT with 4096 points, covering the broad Mn^{4+} EPR peak. The microwave power and modulation amplitude were set to 0.2 mW and 5 G, respectively. Both converse time and time constant were set to 40.96 ms. The spectra were plotted using EasySpin[30] with the assistance of MATLAB. Spectra were normalized according to the weight of samples and measured *Q* values in order to analyze the intensity of all paramagnetic species.

In Situ XRD. An electrode pellet (10 mm diameter, 160 μm thick) was prepared by mixing $Na_2Mn_3O_7$ with carbon black (Cabot, Vulcan XC72R), graphite powder (Alfa Aesar, 99%—300 mesh), and polytetrafluoroethylene powder (Sigma-Aldrich, 1 μm particle size) in a 6:1:1:2 weight ratio. The pellet was assembled into the "AMPIX" electrochemical cell[31] with a glass fiber separator (Whatman GF/A), Na metal foil, and liquid electrolyte [1 M $NaClO_4$ in PC/FEC (98:2

DOI: 10.1021/acs.chemmater.9b00772
Chem. Mater. 2019, 31, 3756−3765

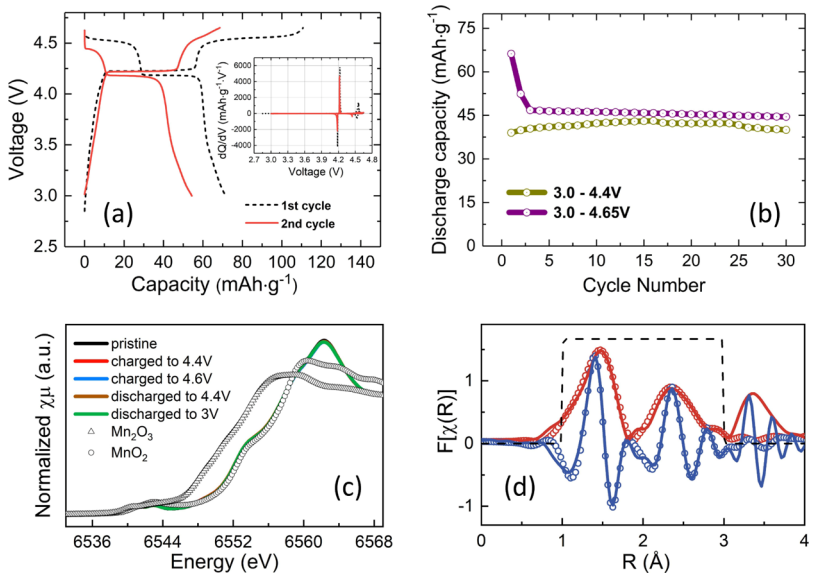

Figure 2. (a) Charge/discharge curves of the initial two cycles of $Na_2Mn_3O_7$ at a cycling rate of C/20 with the corresponding dQ/dV plots shown as an inset. (b) Cycling performance under a rate of C/10 within two different voltage windows. (c) XANES part of Mn K-edge XAS spectra for the pristine and charged samples (charged to 4.4 and 4.6 V, discharged to 4.4 and 3.0 V). Reference spectra of Mn_2O_3 and MnO_2 are also shown to indicate the valence state of the samples, all of which are tetravalent (have similar character to MnO_2). (d) Fitting to both the magnitude and the real part of Fourier-transformed EXAFS spectrum of the pristine sample.

in volume)] within an Ar atmosphere glovebox. A RT galvanostatic charge/discharge experiment was carried out with a cycler (Maccor model 4300) at 8 mA g^{-1} between 4.65 and 3.0 V. Operando XRD data were recorded within the AMPIX cell using high energy X-rays (λ = 0.2113 Å) provided by beamline 11-ID-B at the Advanced Photon Source at Argonne National Laboratory. Diffraction images were recorded at 30 min (or 0.05 Na) intervals in a Debye−Scherrer geometry using an amorphous silicon-based area detector. The data were calibrated using GSAS-II software (0.05−16° 2θ range) using a CeO_2 standard (SRM674b) as calibrant and integrated within GSAS-II.[32]

RESULTS AND DISCUSSION

Structure and Electrochemical Properties of $Na_2Mn_3O_7$. The major diffraction peaks of the as-prepared $Na_2Mn_3O_7$ can be indexed using a structure similar to the refined chalcophanite structure (S.G. $R\bar{3}$). However, extra weak reflections cannot be indexed using this model, instead the space group has to be lowered to $P\bar{1}$ in order to index all Bragg reflections.[22] Rietveld refinement of the structure using synchrotron XRD is shown in Figure 1a,e and Table 1. In the structure one out of every seven Mn sites is vacant on the TM layer. This Mn-vacancy ordering model is further confirmed by the least square refinement of the local structure using neutron PDF (Figures 1b, S2, and Table S1). It is speculated that such local Mn-vacancy ordering would introduce orphaned oxygen 2p orbitals pointing toward the vacancy site as shown in Figure 1f. As a result, the total unhybridized oxygen 2p bands (purple-colored) would be much narrower in the present □−O−Na configuration relative to the Li−O−Li (or Na) configuration in the conventional layered Li (or Na) excess layered cathodes (Figures 1g and S3). In fact, both speculations have been confirmed by the theoretical calculations in the recent reports.[19,20] Though the oxygen follows a distorted P3-type stacking sequence (AABBCC...) in this structure, the two distinct sodium ions are not randomly distributed on the prismatic sites. Instead, one Na^+ ion is found to occupy the distorted prism site (Na1) above and below the vacant Mn site, while the other one occupies the distorted octahedral site (Na2). This unique sodium coordination environment differs drastically from previously reported layered sodium-ion cathodes, where in the single sodium layer sodium ions occupy either the prismatic or the octahedral site, but not both. Thus, the current compound represents a rare example of hybrid sodium coordination environment where half the sodium ions occupy prismatic sites (P) while the other half occupy the octahedral sites (O), which we would like to name as a hybrid P−O system. The refined composition indicates that Mn is in the oxidation state of 4+, which is consistent with the Mn K-edge XAS data (discussed later). TEM images (Figure 1c) clearly show the layer stacking nature of the as-prepared sample, and the corresponding cation arrangements in HRTEM (Figure 1d) are consistent with the refined structure from the synchrotron XRD and neutron PDF.

The electrochemical properties of $Na_2Mn_3O_7$ as SIBs are examined. Figure 2a shows the charge/discharge curves and the corresponding dQ/dV plots of the initial two cycles of $Na_2Mn_3O_7$. 4.65 V was set to be the cut-off voltage in order to explore the plausibility to use all possible charge storage capacity from the oxygen redox, similar to a recent report on $Na_2Mn_3O_7$.[17] The charge and discharge capacities are 111 and 72 mA h g^{-1}, respectively, for the first cycle, but decay to 69 and 55 mA h g^{-1} for the second cycle. However, Coulombic efficiency (CE) of only 65% is observed for the first cycle and 80% for the second cycle. It is likely that this low CE is mainly due to the oxygen gas release from the particle surface (and partially from bulk), similar to various Li-excess materials.[33] In addition, although there is no phase transition during de-intercalation and re-intercalation of Na^+ ions from $Na_2Mn_3O_7$, the original particles became less crystalline and accumulated a significant amounts of stress after the initial cycle, which is evident by the much broaden peaks in the diffraction pattern after discharging to 3.0 V (Figure 4a). Such decrease of crystallinity and increase of stress may also contribute to the poor CE during the first cycle.

DOI: 10.1021/acs.chemmater.9b00772
Chem. Mater. 2019, 31, 3756−3765

Two plateaus emerge at ~4.2 and ~4.5 V with relatively small voltage hysteresis (~40 mV) between charge and discharge curves, indicating an excellent reversibility in view of both crystallographic and electronic structures. The slightly different charge/discharge profiles and capacities compared to the previous studies are presumably due to either the various raw materials or the different synthetic conditions used to prepare the sample. For $Na_xMn_3O_7$, the first desodiation reaction takes place when x reduces from 2.0 to 1.3, while the second one occurs when x reduces from 1.3 to 0.67, as shown in Figure S4. In a similar layered structure $Na_{0.6}Li_{0.2}Mn_{0.8}O_2$, Du et al.[13] and Rong et al.[14] also showed reversible plateaus at 4.2 V (vs Na^+/Na) attributing to a reversible oxygen redox. Thus, it is believed that in $Na_xMn_3O_7$ the crystal chemistry also triggers the oxygen redox. The specific structural feature in this case is the vacancy in the TM layers rather than the Li^+ ions in the previous cases. In fact, this plateau voltage of oxygen redox (~4.2 V) in the Na system perfectly matches its counterpart in a Li system (~4.5 V) because the 0.3 V difference exactly matches the difference of the standard potential between Li^+/Li (−3.04 V) and Na^+/Na (−2.71 V) couples. An ordering between Na ions and Na vacancies and/or various oxygen redox potentials is speculated to be the main reason for the two different charging plateaus. The corresponding structural evolution will be shown with in situ XRD in a later section. Moreover, the 4.5 V plateau is much less reversible than the 4.2 V plateau if comparing the first two cycles. This is even more obvious in Figure 2b, where the cycling data using different charge cut-off voltages tend to merge after just a few cycles. Figure S5a,b compares the corresponding charge/discharge curves upon these cycles. As pointed out by the dashed arrow in Figure S5b, the discharge capacity contributed from the 4.5 V plateau almost vanishes upon a few cycles, while the discharge capacity contributed from the part lower than 4.2 V remains almost constant. Figure S5a highlights the high reversibility of the 4.2 V plateau even though the discharge voltage decays step by step. This observation is reminiscent of the voltage decay phenomenon in the Li-rich Ni−Mn−Co cathodes.[34,35]

Evidence of Oxygen Redox Activity. The XANES part of XAS for the Mn K-edge is shown in Figure 2c. It clearly indicates that in the pristine sample, Mn is tetravalent which can be seen from the spectra comparison among $Na_2Mn_3O_7$, Mn_2O_3, and MnO_2 (all $Na_2Mn_3O_7$ curves fall on top of one another and largely match the behavior of MnO_2). A relatively weak pre-edge indicates that Mn should exclusively occupy the octahedral site in the structure. Interestingly, XAS results show that there is essentially no edge shift observed upon charging, and this is also true for the discharging process. These results strongly suggest that Mn is not involved in the redox reaction and it is very likely that oxygen is solely responsible for the charge/discharge capacity. To better understand the local structure of the pristine sample, Fourier-transformed EXAFS part of XAS is fitted against an O3-type model structure (Figure 2d). After several trials, it is found that a satisfactory fit can only be obtained by considering at least two types of TM−TM shells (which differ by 0.2 Å), reducing the TM−TM coordination number to around 5.3. This is in accordance with the fact that there is a large amount of vacancies in the TM layer, as shown in the refinement using synchrotron XRD (Figure 1a and Table 1) and neutron PDF (Figure 1b and Table S1). A detailed fitting procedure is explained in the Supporting Information.

The oxidation states of Mn and O at the particle surface of $Na_2Mn_3O_7$ upon the first cycle are studied by XPS, and the spectra of Mn 2p and O 1s orbitals are shown in Figure S6a,b. All spectra fittings are based on a binding energy calibration of C 1s orbital to 284.8 eV. The main peak at 642.9 eV in the range of Mn $2p_{3/2}$ core spectra is identified as Mn^{4+} for the pristine sample.[36] The binding energy position of Mn^{4+} did not change during the first cycle, indicating that no obvious redox reaction involved with Mn as shown by the dashed line in Figure S6a. This agrees well with the XANES results. Regarding the O 1s spectra (Figure S6b), the peaks located at 530.2, 531.8, and 533.2 eV are attributed to the lattice O^{2-}, CO_3^{2-} or oxygenated deposited species, and the ClO_4^-, respectively.[14,34,37] The last one at 535.2 eV is possibly a satellite peak due to many body effects from Mn^{7+}−O.[38] Another interesting observation from the change of O 1s spectra is that the peak position shifts to the lower binding energy upon charging and then shifts back upon discharge. The most significant shift is observed for the 4.65 V charged sample, with a 0.36 eV shift relative to the pristine sample. A similar peak shift has been observed in a MoO_{3-x} thin film where vacuum annealing could induce oxygen vacancies at the particle surface. These oxygen vacancies further enlarge the donor levels which may lower the binding energy of the electrons.[39] Accordingly, we speculate that the surface oxygen release might be the reason for such peak shift to a lower binding energy. In fact, in the layered system $Na_{0.6}Li_{0.2}Mn_{0.8}O_2$, such a peak shift is also observed during charge and discharge, implying similar underlying mechanisms of oxygen redox between the two systems.[14]

The CW-EPR shows that pristine $Na_2Mn_3O_7$ powder displays a broad symmetric signal under X-band detection (dashed-green spectrum in C_0 in Figure 3a), which is attributed to the antiferromagnetic Mn^{4+}. The Mn^{4+} EPR signal exhibits a single Lorentzian line shape centered at $g \approx 2.00$.[40,41] In the pristine electrode film, the sharp peak originates from the delocalized electrons within the additive of conductive acetylene black (as demonstrated with black line in C_0 in Figure 3a). Upon charge, desodiation takes place from $Na_2Mn_3O_7$, where O^{2-} must be oxidized to keep charge neutrality. The oxidized oxygen species O_2^{n-} (n = 4, 3, 2, 1, or 0 for O_2 release)[5] change the coupling within the Mn^{4+}−O cluster as demonstrated in C_1 and C_2. The intensity of the 4.4 V sample is slightly weakened when compared to the pristine sample. Greater reduction in intensity was observed for the more charged state at 4.6 V. Six-fold O−Mn hyperfine patterns of the Mn^{4+} mediated by O_2^{n-} was also captured for the first time for the two desodiated samples as marked with light-blue ellipses, which indicates the newly formed $Mn^{4+}-O_2^{n-}$ coupling is anisotropic.[42] To the best of our knowledge, the hyperfine configuration is rarely observed for such Mn^{4+}-based electrode materials.[43−48] This observation is possibly attributed to the vacancy-mediated structure, which shows anisotropy when Na is extracted. Further investigation indicates that the anisotropic configuration is not stable and dynamically relaxed after 7 days as shown in Figure S7. The Mn vacancy site presenting large reversible O-redox is reflected by a stronger Mn−O coupling, which induces slightly reduced EPR integral when compared to Li_2MnO_3 rich sample upon O evolution.[44]

Upon discharge, however, smooth EPR spectra with more restored intensity are found for the resodiated samples (D_1, D_2, and D_3). The fine structure with hyperfine interactions is not observed possibly because the Na^+ intercalation and injection

DOI: 10.1021/acs.chemmater.9b00772
Chem. Mater. 2019, 31, 3756−3765

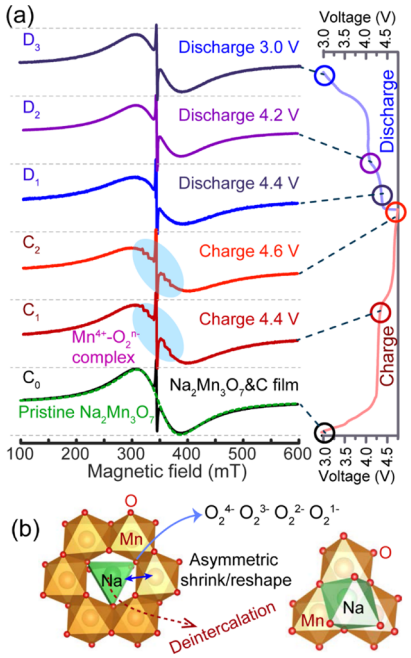

Figure 3. (a) Ex situ CW-EPR spectra for cycled $Na_2Mn_3O_7$ cathodes, spectra are normalized based on cathode mass and measured Q values. The identically separated gray-dashed lines are set to the intensity magnitude of pristine $Na_2Mn_3O_7$ and serve as guidelines to the eye. The sharp peak is assigned to conductive additive. The corresponding electrochemical profile is displayed to the right. (b) Schematic indicates how active O evolution correlates with the possible change of Na−O−Mn configuration.

of electrons show different dynamically synergic effects; or it exhibits faster decay after being stored for half a day in the glovebox (disassembly of cycled batteries and then packing samples). This encourages us to systemically investigate the battery in situ, which will be detailed in a separate contribution. Increased signal is obtained upon discharge, indicating that the reversible O_2^{n-} (n = 4, 3, 2, 1) redox reaction takes place apart from reduction of Mn^{4+} to Mn^{3+} as the latter case would induce weaker EPR signal. This is in good agreement with the previous results from XAS measurements. Finally, the sharp peak of conductive acetylene black does not participate in the EPR evolution upon battery cycling. In short, EPR investigation unambiguously demonstrates that the oxygen anions are actively responsible for the capacity of this cathode material.

Structural Evolution and the Impacts on the Small Voltage Hysteresis. The structure evolution of $Na_2Mn_3O_7$ during the initial charge/discharge cycle was tracked via in situ XRD (Figure 4). The detailed crystal structure changes can be readily followed through the disappearance and reappearance of certain low intensity reflections. We find that the very strong preferred orientation of the in situ data hinders accurate structure refinement (e.g. Rietveld refinement), but the well-defined Bragg diffraction peak positions enable symmetry identification and lattice parameter refinements using parametric Le Bail fits. Visually from the waterfall plot shown in Figure 4a, it is evident that there are two apparent stages during the first charge. In stage C1 (4.2 V plateau), the refined lattice parameters of the triclinic unit cell (S.G. $P\bar{1}$) barely change although Na ions are continuously de-intercalated from the structure (as evidenced by the simultaneous increase of the charge capacity). The total volume decrease during this charge stage is less than 0.1% (~4‰), indicating that it is an essentially zero-strain process. According to simulation done separately, it is very likely that Na2 site (the octahedral site) is the first vacant sodium site while the Na1 site (the prism coordinated site) is well maintained (Figure S8). This can be attributed to the much higher cation−cation repulsion on the octahedral site. It is also worth noting that only ~80% Na^+ (specific capacity of 65 mA h g^{-1}) was extracted from the octahedral site in stage C1.

In contrast, an immediate two-phase reaction occurs on further extraction of Na^+ from the structure (switching from the 4.2 V plateau to the 4.5 V plateau). This is seen with the vanishing $(001)_{triclinic}$ peak while a new peak arises at much smaller d-spacing (or higher 2θ angle). It is worth noting that the d-spacing associated with the $(001)_{triclinic}$ peak reflects the dimension of the $Mn_{6/7}\square_{1/7}O_2$ plane, as can be seen in Figure S9. Therefore, the drastic decrease of the d-spacing associated with the 001 reflection indicates the shrinking of the $Mn_{6/7}\square_{1/7}O_2$ plane. This could be an effect of either the decrease of Mn−O bond distances (e.g. resulting from the oxidation of Mn^{4+}) or the shrinkage of the vacant MnO_6 octahedron. The former is unlikely to occur in the current system because the valence of Mn^{4+} is well maintained throughout the entire charging process (Mn K-edge XANES in Figure 2c). Thus, it is very likely that removal of more than 0.8 Na^+ leads to the shrinkage of the vacant MnO_6 octahedron (as illustrated in Figure S9) and the rearrangement of the residual Na^+. It is also expected that this dimension lessening results in the asymmetric coupling between the oxidized oxygen ions (likely to be short interlayer O−O pairs)[14,49] and Mn^{4+} surrounding the vacant site. This asymmetrically coupled Mn−O complex may be the underlying reason for the observed six-fold hyperfine structure observed in the EPR (Figure 3). A more detailed local structure investigation (e.g., via neutron PDF) is required to draw a more comprehensive conclusion.

Moreover, the disappearance of extra diffraction peaks such as (11−1), (101), and (020) (highlighted in the patterns of Figure 4a) suggests an increase of the crystallographic symmetry of the desodiated phase. This is indeed confirmed by pattern indexing, which reveals that the remaining Bragg reflections can be effectively indexed using the space group $R3$ with refined lattice parameter a = 7.4740 (16) Å and c = 16.5033(99) Å, similar to that of the dehydrated layered chalcophanite but with the centrosymmetry lifted (the oxygen ions follow the O3-type stacking in the dehydrated chalcophanite but show the P3-type stacking sequences in the current charged phase).[50,51] However, substantial distortion exists, as evidenced by the position mismatch of some reflections when refining against the proposed space group (see highlight in Figure S10a). This distortion can be modeled by introducing monoclinic shearing (see highlight in Figure S10b), a common phenomenon observed for various layered oxide cathodes.[52,53] It turns out that the pattern can be modeled using the S.G. Cm with refined lattice parameter of a = 7.2957(24) Å, b = 12.4916(56) Å, c = 5.8448(8) Å, and β = 106.328(14)°. This increase of structure symmetry after the first charge stage (C1) is further confirmed by ^{23}Na NMR spectra (Figure 5): two distinct sodium environments are identified in the pristine state, corresponding to the two different sodium sites (with prismatic and octahedral coordination, Figure 4c). The 14 ppm peak (Na2) vanishes

DOI: 10.1021/acs.chemmater.9b00772
Chem. Mater. 2019, 31, 3756−3765

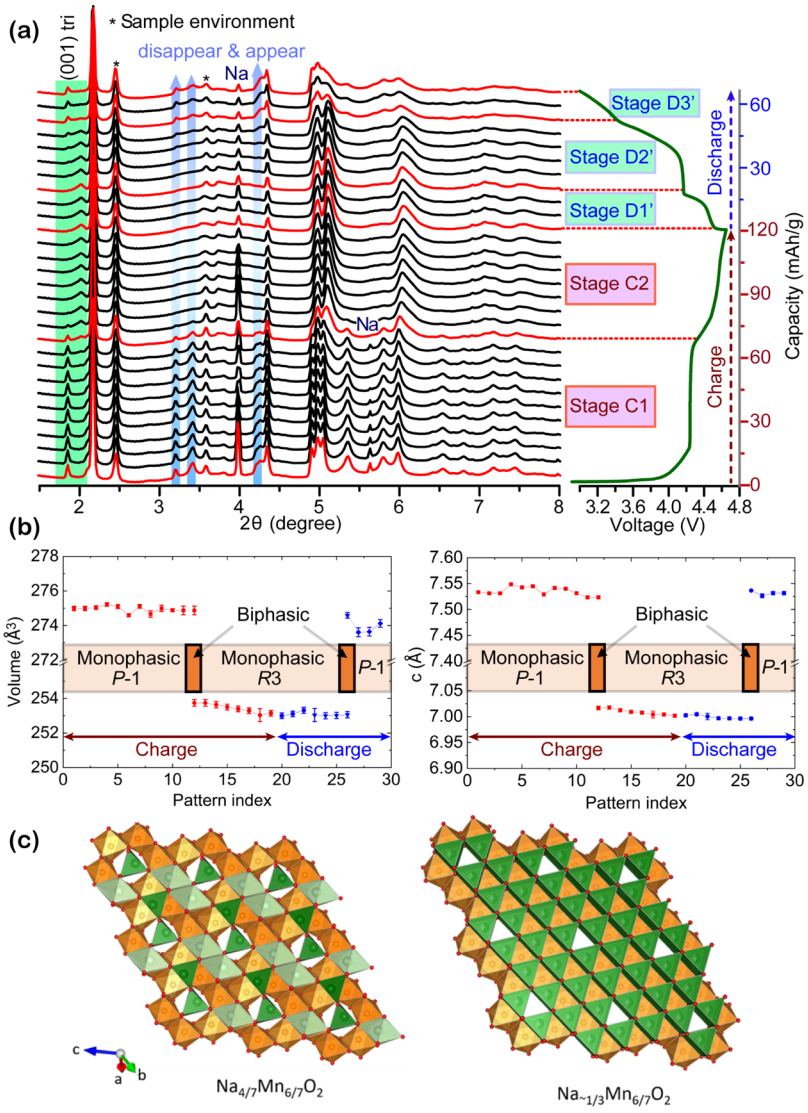

Figure 4. (a) In situ synchrotron XRD and lattice parameter evolution of $Na_2Mn_3O_7$ during the initial charge/discharge cycle. (b) Unit cell volume and lattice parameter c (using triclinic S.G. $P\bar{1}$ for straightforward comparison across phase transitions) refined using in situ XRD patterns. (c) Coordination environments of sodium ions in the pristine sample and the sample charged to 4.2 V. The amount of residual Na^+ was estimated from the charge capacity.

after charging to 4.2 V while the −2.8 ppm peak (Na1) is reserved but becomes significantly sharper, indicating that one of the sodium ion environments is maintained but with much higher mobility (or higher hopping frequency). This can be attributed to the increased symmetry in the sodium depopulated phase that possesses the degenerated prismatic sites for Na^+. It is also possible that the remaining Na^+ ions occupy two different prism sites but with the Na^+ exchange rate (between the two sites) higher than the NMR time scale, as can be seen in Figure 4c. The conclusion is fully consistent with previous literature reports on the P2-$Na_x[Li_yNi_zMn_{1-y-z}]O_2$ ($0 < x, y, z < 1$).[54,55]

In order to better monitor the lattice parameter evolution (especially the volume change) throughout the initial charge/discharge, the original triclinic space group $P\bar{1}$ (instead of the trigonal or monoclinic space group) was adopted for the parametric Le Bail fits of the in situ diffraction patterns (as seen in Figures 4b,c, and S11). A similar reversible lattice parameter evolution was observed during the initial discharge, though three different stages are apparent instead of two. Stage D1′ is a reversible process of sodiation with small volume change, despite a significant decrease in amount of Na^+ ions that are re-intercalated relative to the levels of initial de-intercalation. During the stage D2′, a two-phase reaction proceeds where the $(001)_{triclinic}$ peak vanishes while the peak at much lower 2θ grows back in, indicating that Na ions start to re-occupy the distorted octahedral site with symmetry lowering to the original triclinic S.G. $P\bar{1}$. This is further confirmed by the recovery of the triclinic (11−1), (101), and (020) reflections (highlighted in the patterns of Figure 4a). In stage D3′, the intensity of $(001)_{triclinic}$ peak increases slightly as further intercalation of Na^+ ions proceeds. Taken together, these observations suggest that the de-intercalation and re-intercalation of sodium ions in the current structure only affects the dimension of the TM plane, while barely changing the overall stacking sequences of oxygen ions, that is the near P3-type stacking (AABBCC...) of oxygen ions are well maintained. In addition, the interlayer distance along the layer stacking direction is also well maintained through the entire charge/discharge process, as evidenced by the well-

DOI: 10.1021/acs.chemmater.9b00772
Chem. Mater. 2019, 31, 3756−3765

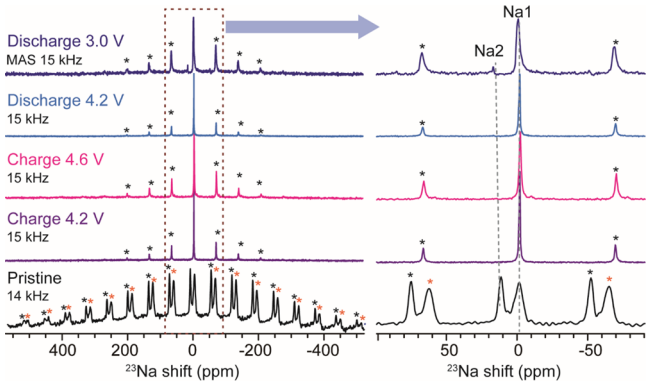

Figure 5. ^{23}Na magic-angle-spinning (MAS) NMR spectra of NMO electrodes at different cycling states. Isotropic peaks with the first order of spinning side bands (SSBs) are enlarged to the right. Asterisks indicate SSBs. The ^{23}Na MAS NMR experiments were performed on a Bruker AVANCE III spectrometer in a 19.5 T magnetic field. Electrodes were packed into 3.2 mm rotors and spun at a MAS rate of 14 or 15 kHz as noted to each spectrum. The recycle delay was 1.0 s and the 90° pulse length was 1.6 μs. $NaCl_{(s)}$ with a ^{23}Na chemical shift at 7.21 ppm was used as a reference. The pristine sample shows large anisotropy up to 1000 ppm for full spectral width (covering all SSBs), with two distinguished isotopic peaks at 14 ppm (Na2) and −2.8 ppm (Na1). The cycled electrodes have relatively small anisotropy of ∼500 ppm and larger mobility as reflected with narrower line-width. The presented vacancy with such special configuration induces much smaller Fermi effect on Na atoms compared to the reported electrodes.[55,58]

maintained diffraction peak at around 2θ = 2.17° (003 reflection for the trigonal S.G. *R*3 or the 10−1 reflection for the triclinic S.G. $P\bar{1}$). This is in clear contrast to many P-type sodium layered oxide cathodes, where the removal of appreciable amounts of sodium ions often leads to the irreversible P-type to O-type phase transition and simultaneous decrease of the interlayer distances.[53,56,57] Taken together, the degree of voltage hysteresis associated with lattice oxygen redox is most likely determined by two strongly correlated factors. First, if an irreversible gliding of oxygen layers occurs during the de-intercalation of Li^+ or Na^+, the voltage hysteresis is often very large. Second, if there is irreversible cation migration from TM layer to the Li/Na layer, the voltage hysteresis is also significant. However, it is worth noting that the irreversible gliding of oxygen layers is often correlated with or enhanced by the cation migration, such as in P3-type $Na_{2/3}Mg_{1/3}Mn_{2/3}O_2$.[53] Therefore, it is unlikely that the oxygen stacking sequence alone determines the extent of the voltage hysteresis. However, they may be correlated to a certain level. This implies that although the P-type structure indeed helps on maintaining the structural integrity, it does not guarantee small voltage hysteresis. Avoiding cation migration (or at least irreversible cation migration) is also indispensable for achieving the small voltage hysteresis when using lattice oxygen redox.

CONCLUSIONS

$Na_2Mn_3O_7$ is demonstrated to work as a promising cathode for sodium-ion batteries using only lattice oxygen redox. The cause of minimal voltage hysteresis between the initial charge and discharge curve is likely to be rooted in the well-maintained oxygen stacking sequence in the absence of irreversible gliding of oxygen layers or cation migration from the TM layer. The partial depopulation of the Na^+ from the octahedrally coordinated site is an essentially zero strain process, as evidenced by the very small volume decrease (less than 0.1%). The shrinking of the vacant MnO_6 octahedra upon charging is identified as the major driving force for the large volume decrease when Na^+ is removed from the prismatic sites. This discovery paves a new route to achieve lattice oxygen redox in layered oxide cathodes without introducing large voltage hysteresis, and hence it may inspire the exploration of new cathode materials that can achieve both high energy density and efficiency by using lattice anionic redox.

ASSOCIATED CONTENT

Supporting Information

The Supporting Information is available free of charge on the ACS Publications website at DOI: 10.1021/acs.chemmater.9b00772.

Fitting description of EXAFS for pristine $Na_2Mn_3O_7$, refined pattern and structural information using neutron PDF, crystal structure of $ZnMn_3O_7$, small-box least square refinement of the intermediate range structure of $Na_2Mn_3O_7$ using the neutron pair distribution function, molecular orbitals and band structure of the conventional layered TM oxides, voltage profile versus specific capacity and Na composition *x* of $Na_xMn_3O_7$, charge/discharge voltage profiles, XPS spectra, CW-EPR spectra for the stored samples, simulated XRD patterns, structural illustrations, and refined lattice parameters (PDF)

AUTHOR INFORMATION

Corresponding Authors

*E-mail: liuj1@ornl.gov (J.L.).
*E-mail: nandaj@ornl.gov (J.N.).
*E-mail: pagekl@ornl.gov (K.P.).
*E-mail: ashfia.huq@gmail.com (A.H.).

ORCID

Bohang Song: 0000-0002-6477-609X
Enyuan Hu: 0000-0002-1881-4534
Yiman Zhang: 0000-0002-5468-7181
Nathan D. Phillip: 0000-0002-6223-8765
Cheng Li: 0000-0002-6546-6413
Yan-Yan Hu: 0000-0003-0677-5897
Miaofang Chi: 0000-0003-0764-1567
Gabriel M. Veith: 0000-0002-5186-4461
Xiao-Qing Yang: 0000-0002-3625-3478
Jue Liu: 0000-0002-4453-910X
Jagjit Nanda: 0000-0002-6875-0057
Katharine Page: 0000-0002-9071-3383

Author Contributions

▲B.S. and M.T. contributed equally to this work. J.L. conceived the idea; J.L. and B.S. designed the experiments and wrote the manuscript together with M.T. and E.H. J.N., K.P., and A.H. guided the research. M.T., L.S., and Y.-Y.H. performed the EPR characterizations and analyzed the data. E.H., Z.S., and X.-Q.Y. carried out the XAS experiments and analyzed the data. B.S., O.J.B., K.M.W., and C.L. performed the in situ XRD experiments. J.L. collected the neutron diffraction data and carried out the structure analysis. X.L. and M.C. did characterization using TEM. B.S., Y.Z., and G.M.V. carried out the electrochemistry testings. B.S., N.D.P., and G.M.V.

DOI: 10.1021/acs.chemmater.9b00772
Chem. Mater. 2019, 31, 3756−3765

performed the XPS characterizations. All authors contributed to the manuscript preparation.

Notes

The authors declare no competing financial interest.

■ ACKNOWLEDGMENTS

This research is primarily supported by the U.S. Department of Energy, Office of Science, Office of Basic Energy Sciences, Early Career Research Program award KC040602, under contract number DE-AC05-00OR22725. Research conducted at the NOMAD beamline at ORNL's Spallation Neutron Source was sponsored by the Scientific User Facilities Division, Office of Basic Sciences, U.S. Department of Energy. All EPR measurements were performed at the NHMFL, which is supported by National Science Foundation Cooperative agreement nos. DMR-1157490 and DMR-1644779. E.H., Z.S., and X.-Q.Y. were supported by the Assistant Secretary for Energy Efficiency and Renewable Energy, Vehicle Technologies Office of the U.S. DOE through the Advanced Battery Materials Research (BMR) Program, including Battery500 consortium under contract DE-SC0012704. J.N. was sponsored by the Office of Energy Efficiency and Renewable Energy (EERE) Vehicle Technologies Office (VTO). This research used beamline ISS 8-ID of the National Synchrotron Light Source II, a U.S. Department of Energy (DOE) Office of Science User Facility operated for the DOE Office of Science by Brookhaven National Laboratory under contract no. DE-SC0012704. Electron microscopy work was performed at Oak Ridge National Laboratory's Center for Nanophase Materials Sciences, which is a U.S. DOE Office of Science User Facility (M.C. & X.L.). N.D.P., G.M.V., M.C., and X.L. were supported by the U.S. Department of Energy, Office of Basic Energy Sciences, Division of Materials Science and Engineering. This research used 11-BM, 11-ID-B beamline and electrochemistry laboratory resources of the Advanced Photon Source, a U.S. Department of Energy (DOE) Office of Science User Facility operated for the DOE Office of Science by Argonne National Laboratory under contract no. DE-AC02-06CH11357.

■ REFERENCES

(1) Luo, K.; Roberts, M. R.; Hao, R.; Guerrini, N.; Pickup, D. M.; Liu, Y.-S.; Edström, K.; Guo, J.; Chadwick, A. V.; Duda, L. C.; Bruce, P. G. Charge-compensation in 3d-transition-metal-oxide intercalation cathodes through the generation of localized electron holes on oxygen. *Nat. Chem.* **2016**, *8*, 684−691.

(2) Assat, G.; Tarascon, J.-M. Fundamental understanding and practical challenges of anionic redox activity in Li-ion batteries. *Nat. Energy* **2018**, *3*, 373−386.

(3) Perez, A. J.; Jacquet, Q.; Batuk, D.; Iadecola, A.; Saubanère, M.; Rousse, G.; Larcher, D.; Vezin, H.; Doublet, M.-L.; Tarascon, J.-M. Approaching the limits of cationic and anionic electrochemical activity with the Li-rich layered rocksalt Li_3IrO_4. *Nat. Energy* **2017**, *2*, 954−962.

(4) Freire, M.; Kosova, N. V.; Jordy, C.; Chateigner, D.; Lebedev, O. I.; Maignan, A.; Pralong, V. A new active Li-Mn-O compound for high energy density Li-ion batteries. *Nat. Mater.* **2016**, *15*, 173−177.

(5) Sathiya, M.; Rousse, G.; Ramesha, K.; Laisa, C. P.; Vezin, H.; Sougrati, M. T.; Doublet, M.-L.; Foix, D.; Gonbeau, D.; Walker, W.; Prakash, A. S.; Ben Hassine, M.; Dupont, L.; Tarascon, J.-M. Reversible anionic redox chemistry in high-capacity layered-oxide electrodes. *Nat. Mater.* **2013**, *12*, 827−835.

(6) Yabuuchi, N.; Takeuchi, M.; Nakayama, M.; Shiiba, H.; Ogawa, M.; Nakayama, K.; Ohta, T.; Endo, D.; Ozaki, T.; Inamasu, T.; Sato, K.; Komaba, S. High-capacity electrode materials for rechargeable lithium batteries: Li_3NbO_4-based system with cation-disordered rocksalt structure. *Proc. Natl. Acad. Sci. U.S.A.* **2015**, *112*, 7650−7655.

(7) Zhao, E.; Li, Q.; Meng, F.; Liu, J.; Wang, J.; He, L.; Jiang, Z.; Zhang, Q.; Yu, X.; Gu, L.; Yang, W.; Li, H.; Wang, F.; Huang, X. Stabilizing the oxygen lattice and reversible oxygen redox chemistry through structural dimensionality in lithium-rich cathode oxides. *Angew. Chem., Int. Ed.* **2019**, *58*, 4323−4327.

(8) Hong, J.; Gent, W. E.; Xiao, P.; Lim, K.; Seo, D.-H.; Wu, J.; Csernica, P. M.; Takacs, C. J.; Nordlund, D.; Sun, C.-J.; Stone, K. H.; Passarello, D.; Yang, W.; Prendergast, D.; Ceder, G.; Toney, M. F.; Chueh, W. C. Metal−oxygen decoordination stabilizes anion redox in Li-rich oxides. *Nat. Mater.* **2019**, *18*, 256−265.

(9) Li, W.; Song, B.; Manthiram, A. High-voltage positive electrode materials for lithium-ion batteries. *Chem. Soc. Rev.* **2017**, *46*, 3006−3059.

(10) Hy, S.; Liu, H.; Zhang, M.; Qian, D.; Hwang, B.-J.; Meng, Y. S. Performance and design considerations for lithium excess layered oxide positive electrode materials for lithium ion batteries. *Energy Environ. Sci.* **2016**, *9*, 1931−1954.

(11) Jacquet, Q.; Iadecola, A.; Saubanère, M.; Lemarquis, L.; Berg, E. J.; Alves Dalla Corte, D.; Rousse, G.; Doublet, M.-L.; Tarascon, J.-M. Competition between metal dissolution and gas release in Li-rich $Li_3Ru_yIr_{1-y}O_4$ model compounds showing anionic redox. *Chem. Mater.* **2018**, *30*, 7682−7690.

(12) Pearce, P. E.; Perez, A. J.; Rousse, G.; Saubanère, M.; Batuk, D.; Foix, D.; McCalla, E.; Abakumov, A. M.; Van Tendeloo, G.; Doublet, M.-L.; Tarascon, J.-M. Evidence for anionic redox activity in a tridimensional-ordered Li-rich positive electrode beta-Li_2IrO_3. *Nat. Mater.* **2017**, *16*, 580−586.

(13) Du, K.; Zhu, J.; Hu, G.; Gao, H.; Li, Y.; Goodenough, J. B. Exploring reversible oxidation of oxygen in a manganese oxide. *Energy Environ. Sci.* **2016**, *9*, 2575−2577.

(14) Rong, X.; Liu, J.; Hu, E.; Liu, Y.; Wang, Y.; Wu, J.; Yu, X.; Page, K.; Hu, Y.-S.; Yang, W.; Li, H.; Yang, X.-Q.; Chen, L.; Huang, X. Structure-induced reversible anionic redox activity in Na layered oxide cathode. *Joule* **2018**, *2*, 125−140.

(15) Shannon, R. D. Revised effective ionic-radii and systematic studies of interatomic distances in halides and chalcogenides. *Acta Crystallogr., Sect. A: Cryst. Phys., Diffr., Theor. Gen. Crystallogr.* **1976**, *32*, 751−767.

(16) Seo, D.-H.; Lee, J.; Urban, A.; Malik, R.; Kang, S.; Ceder, G. The structural and chemical origin of the oxygen redox activity in layered and cation-disordered Li-excess cathode materials. *Nat. Chem.* **2016**, *8*, 692−697.

(17) Post, J. E.; Appleman, D. E. Chalcophanite, $ZnMn_3O_7{\bullet}3H_2O$-new crystal-structure determinations. *Am. Mineral.* **1988**, *73*, 1401−1404.

(18) Liu, J.; Yu, L.; Hu, E.; Guiton, B. S.; Yang, X.-Q.; Page, K. Large-scale synthesis and comprehensive structure study of delta-MnO_2. *Inorg. Chem.* **2018**, *57*, 6873−6882.

(19) de Boisse, B. M.; Nishimura, S.; Watanabe, E.; Lander, L.; Tsuchimoto, A.; Kikkawa, J.; Kobayashi, E.; Asakura, D.; Okubo, M.; Yamada, A. Highly reversible oxygen-redox chemistry at 4.1 V in $Na_{4/7-x}[\square_{1/7}Mn_{6/7}]O_2$ (□: Mn vacancy). *Adv. Energy Mater.* **2018**, *8*, 1800409.

(20) Li, Y.; Wang, X.; Gao, Y.; Zhang, Q.; Tan, G.; Kong, Q.; Bak, S.; Lu, G.; Yang, X.-Q.; Gu, L.; Lu, J.; Amine, K.; Wang, Z.; Chen, L. Native vacancy enhanced oxygen redox reversibility and structural robustness. *Adv. Energy Mater.* **2018**, *9*, 1803087.

(21) Wang, Q.; Yang, W.; Kang, F.; Li, B. $Na_2Mn^{3+}{}_{0.3}Mn^{4+}{}_{2.7}O_{6.85}$: A cathode with simultaneous cationic and anionic redox in Na-ion battery. *Energy Storage Mater.* **2018**, *14*, 361−366.

(22) Adamczyk, E.; Pralong, V. $Na_2Mn_3O_7$: A suitable electrode material for Na-ion batteries? *Chem. Mater.* **2017**, *29*, 4645−4648.

(23) Coelho, A. A.; Chater, P. A.; Kern, A. Fast synthesis and refinement of the atomic pair distribution function. *J. Appl. Crystallogr.* **2015**, *48*, 869−875.

DOI: 10.1021/acs.chemmater.9b00772
Chem. Mater. 2019, 31, 3756−3765

(24) Cheary, R. W.; Coelho, A. A.; Cline, J. P. Fundamental Parameters Line Profile Fitting in Laboratory Diffractometers. *J. Res. Natl. Inst. Stand. Technol.* **2004**, *109*, 1−25.
(25) Neuefeind, J.; Feygenson, M.; Carruth, J.; Hoffmann, R.; Chipley, K. K. The nanoscale ordered materials diffractometer NOMAD at the Spallation Neutron Source SNS. *Nucl. Instrum. Methods Phys. Res., Sect. B* **2012**, *287*, 68−75.
(26) Toby, B. H.; Egami, T. Accuracy of pair distribution function analysis applied to crystalline and non-crystalline materials. *Acta Crystallogr., Sect. A: Found. Crystallogr.* **1992**, *48*, 336−346.
(27) Farrow, C. L.; Juhas, P.; Liu, J. W.; Bryndin, D.; Božin, E. S.; Bloch, J.; Proffen, T.; Billinge, S. J. L. PDFfit2 and PDFgui: computer programs for studying nanostructure in crystals. *J. Phys.: Condens. Matter* **2007**, *19*, 335219.
(28) Chung, J. S.; Thorpe, M. F. Local atomic structure of semiconductor alloys using pair distribution functions. *Phys. Rev. B* **1997**, *55*, 1545−1553.
(29) Ravel, B.; Newville, M. ATHENA, ARTEMIS, HEPHAESTUS: data analysis for X-ray absorption spectroscopy using IFEFFIT. *J. Synchrotron Radiat.* **2005**, *12*, 537−541.
(30) Stoll, S.; Schweiger, A. EasySpin, a comprehensive software package for spectral simulation and analysis in EPR. *J. Magn. Reson.* **2006**, *178*, 42−55.
(31) Borkiewicz, O. J.; Shyam, B.; Wiaderek, K. M.; Kurtz, C.; Chupas, P. J.; Chapman, K. W. The AMPIX electrochemical cell: a versatile apparatus for in situ X-ray scattering and spectroscopic measurements. *J. Appl. Crystallogr.* **2012**, *45*, 1261−1269.
(32) Toby, B. H.; Von Dreele, R. B. GSAS-II: the genesis of a modern open-source all purpose crystallography software package. *J. Appl. Crystallogr.* **2013**, *46*, 544−549.
(33) Yabuuchi, N.; Yoshii, K.; Myung, S.-T.; Nakai, I.; Komaba, S. Detailed Studies of a High-Capacity Electrode Material for Rechargeable Batteries, Li_2MnO_3−$LiCo_{1/3}Ni_{1/3}Mn_{1/3}O_2$. *J. Am. Chem. Soc.* **2011**, *133*, 4404−4419.
(34) Sathiya, M.; Abakumov, A. M.; Foix, D.; Rousse, G.; Ramesha, K.; Saubanère, M.; Doublet, M. L.; Vezin, H.; Laisa, C. P.; Prakash, A. S.; Gonbeau, D.; VanTendeloo, G.; Tarascon, J.-M. Origin of voltage decay in high-capacity layered oxide electrodes. *Nat. Mater.* **2015**, *14*, 230−238.
(35) Song, B.; Liu, Z.; Lai, M. O.; Lu, L. Structural evolution and the capacity fade mechanism upon long-term cycling in Li-rich cathode material. *Phys. Chem. Chem. Phys.* **2012**, *14*, 12875−12883.
(36) Biesinger, M. C.; Payne, B. P.; Grosvenor, A. P.; Lau, L. W. M.; Gerson, A. R.; Smart, R. S. C. Resolving surface chemical states in XPS analysis of first row transition metals, oxides and hydroxides: Cr, Mn, Fe, Co and Ni. *Appl. Surf. Sci.* **2011**, *257*, 2717−2730.
(37) Beard, B. C. Sodium salts of chlorine oxyacid anions, Cl(+7), perchlorate, XPS comparison spectra. *Surf. Sci. Spectra* **1993**, *2*, 97−103.
(38) Oku, M. X-ray photoelectron-spectra of $KMnO_4$ and K_2MnO_4 fractured in-situ. *J. Electron Spectrosc. Relat. Phenom.* **1995**, *74*, 135−148.
(39) Anwar, M.; Hogarth, C. A.; Bulpett, R. Effect of substrate-temperature and film thickness on the surface-structure of some thin amorphous films of MoO_3 studied by X-ray photoelectron-spectroscopy (Esca). *J. Mater. Sci.* **1989**, *24*, 3087−3090.
(40) Stoyanova, R.; Gorova, M.; Zhecheva, E. EPR monitoring of Mn^{4+} distribution in $Li_4Mn_5O_{12}$ spinels. *J. Phys. Chem. Solids* **2000**, *61*, 615−620.
(41) Kalapsazova, M.; Ivanova, S.; Kukeva, R.; Simova, S.; Wegner, S.; Zhecheva, E.; Stoyanova, R. Combined use of EPR and Na-23 MAS NMR spectroscopy for assessing the properties of the mixed cobalt-nickel-manganese layers of P3-$Na_yCo_{1-2x}Ni_xMn_xO_2$. *Phys. Chem. Chem. Phys.* **2017**, *19*, 27065−27073.
(42) Gupta, R.; Taguchi, T.; Lassalle-Kaiser, B.; Bominaar, E. L.; Yano, J.; Hendrich, M. P.; Borovik, A. S. High-spin Mn-oxo complexes and their relevance to the oxygen-evolving complex within photosystem II. *Proc. Natl. Acad. Sci. U.S.A.* **2015**, *112*, 5319−5324.
(43) Krzystek, J.; Ozarowski, A.; Telser, J. Multi-frequency, high-field EPR as a powerful tool to accurately determine zero-field splitting in high-spin transition metal coordination complexes. *Coord. Chem. Rev.* **2006**, *250*, 2308−2324.
(44) Tang, M.; Dalzini, A.; Li, X.; Feng, X.; Chien, P.-H.; Song, L.; Hu, Y.-Y. Operando EPR for simultaneous monitoring of anionic and cationic redox processes in Li-rich metal oxide cathodes. *J. Phys. Chem. Lett.* **2017**, *8*, 4009−4016.
(45) Stoyanova, R.; Gorova, M.; Zhecheva, E. EPR of Mn^{4+} in spinels $Li_{1+x}Mn_{2-x}O_4$ with $0 \leq x \leq 0.1$. *J. Phys. Chem. Solids* **2000**, *61*, 609−614.
(46) Zhecheva, E.; Stoyanova, R.; Alcántara, R.; Lavela, P.; Tirado, J. L. EPR studies of Li deintercalation from $LiCoMnO_4$ spinel-type electrode active material. *J. Power Sources* **2006**, *159*, 1389−1394.
(47) Stoyanova, R.; Zhecheva, E.; Vassilev, S. Mn^{4+} environment in layered $Li[Mg_{0.5-x}Ni_xMn_{0.5}]O_2$ oxides monitored by EPR spectroscopy. *J. Solid State Chem.* **2006**, *179*, 378−388.
(48) Stoyanova, R.; Ivanova, S.; Zhecheva, E.; Samoson, A.; Simova, S.; Tzvetkova, P.; Barra, A.-L. Correlations between lithium local structure and electrochemistry of layered $LiCo_{1-2x}Ni_xMn_xO_2$ oxides: Li-7 MAS NMR and EPR studies. *Phys. Chem. Chem. Phys.* **2014**, *16*, 2499−2507.
(49) McCalla, E.; Abakumov, A. M.; Saubanere, M.; Foix, D.; Berg, E. J.; Rousse, G.; Doublet, M.-L.; Gonbeau, D.; Novak, P.; Van Tendeloo, G.; Dominko, R.; Tarascon, J.-M. Visualization of O-O peroxo-like dimers in high-capacity layered oxides for Li-ion batteries. *Science* **2015**, *350*, 1516−1521.
(50) Post, J. E.; Heaney, P. J. Time-resolved synchrotron X-ray diffraction study of the dehydration behavior of chalcophanite. *Am. Mineral.* **2014**, *99*, 1956−1961.
(51) Chen, R.; Zavalij, P.; Whittingham, M. S. Hydrothermal synthesis and characterization of $K_xMnO_2 \cdot yH_2O$. *Chem. Mater.* **1996**, *8*, 1275−1280.
(52) Liu, J.; Yin, L.; Wu, L.; Bai, J.; Bak, S.-M.; Yu, X.; Zhu, Y.; Yang, X.-Q.; Khalifah, P. G. Quantification of honeycomb number-type stacking faults: application to $Na_3Ni_2BiO_6$ cathodes for Na-ion batteries. *Inorg. Chem.* **2016**, *55*, 8478−8492.
(53) Song, B. H.; Hu, E. Y.; Liu, J.; Zhang, Y. M.; Yang, X.-Q.; Nanda, J.; Huq, A.; Page, K. A novel P3-type $Na_{2/3}Mg_{1/3}Mn_{2/3}O_2$ as high capacity sodium-ion cathode using reversible oxygen redox. *J. Mater. Chem. A* **2019**, *7*, 1491−1498.
(54) Xu, J.; Lee, D. H.; Clément, R. J.; Yu, X.; Leskes, M.; Pell, A. J.; Pintacuda, G.; Yang, X.-Q.; Grey, C. P.; Meng, Y. S. Identifying the critical role of Li substitution in P2-$Na_x[Li_yNi_zMn_{1-y-z}]O_2$ ($0 < x, y, z < 1$) intercalation cathode materials for high-energy Na-ion batteries. *Chem. Mater.* **2014**, *26*, 1260−1269.
(55) Clément, R. J.; Xu, J.; Middlemiss, D. S.; Alvarado, J.; Ma, C.; Meng, Y. S.; Grey, C. P. Direct evidence for high Na^+ mobility and high voltage structural processes in P2-$Na_x[Li_yNi_zMn_{1-y-z}]O_2$ ($x, y, z \leq 1$) cathodes from solid-state NMR and DFT calculations. *J. Mater. Chem. A* **2017**, *5*, 4129−4143.
(56) Maitra, U.; House, R. A.; Somerville, J. W.; Tapia-Ruiz, N.; Lozano, J. G.; Guerrini, N.; Hao, R.; Luo, K.; Jin, L.; Pérez-Osorio, M. A.; Massel, F.; Pickup, D. M.; Ramos, S.; Lu, X.; McNally, D. E.; Chadwick, A. V.; Giustino, F.; Schmitt, T.; Duda, L. C.; Roberts, M. R.; Bruce, P. G. Oxygen redox chemistry without excess alkali-metal ions in $Na_{2/3}[Mg_{0.28}Mn_{0.72}]O_2$. *Nat. Chem.* **2018**, *10*, 288−295.
(57) Yabuuchi, N.; Kajiyama, M.; Iwatate, J.; Nishikawa, H.; Hitomi, S.; Okuyama, R.; Usui, R.; Yamada, Y.; Komaba, S. P2-type $Na_x[Fe_{1/2}Mn_{1/2}]O_2$ made from earth-abundant elements for rechargeable Na batteries. *Nat. Mater.* **2012**, *11*, 512−517.
(58) Ma, C.; Alvarado, J.; Xu, J.; Clément, R. J.; Kodur, M.; Tong, W.; Grey, C. P.; Meng, Y. S. Exploring oxygen activity in the high energy P2-type $Na_{0.78}Ni_{0.23}Mn_{0.69}O_2$ cathode material for Na-ion batteries. *J. Am. Chem. Soc.* **2017**, *139*, 4835−4845.

DOI: 10.1021/acs.chemmater.9b00772
Chem. Mater. 2019, 31, 3756−3765